Ultralight Metallic Microlattices

T. A. Schaedler, *et al.*

Science **334**, 962 (2011);
DOI: 10.1126/science.1211649

Ultralight Metallic Microlattices

T. A. Schaedler,[1]* A. J. Jacobsen,[1] A. Torrents,[2] A. E. Sorensen,[1] J. Lian,[3] J. R. Greer,[3] L. Valdevit,[2] W. B. Carter[1]

Ultralight (<10 milligrams per cubic centimeter) cellular materials are desirable for thermal insulation; battery electrodes; catalyst supports; and acoustic, vibration, or shock energy damping. We present ultralight materials based on periodic hollow-tube microlattices. These materials are fabricated by starting with a template formed by self-propagating photopolymer waveguide prototyping, coating the template by electroless nickel plating, and subsequently etching away the template. The resulting metallic microlattices exhibit densities $\rho \geq 0.9$ milligram per cubic centimeter, complete recovery after compression exceeding 50% strain, and energy absorption similar to elastomers. Young's modulus E scales with density as $E \sim \rho^2$, in contrast to the $E \sim \rho^3$ scaling observed for ultralight aerogels and carbon nanotube foams with stochastic architecture. We attribute these properties to structural hierarchy at the nanometer, micrometer, and millimeter scales.

The effective properties of low-density materials are defined both by their cellular architecture (i.e., the spatial configuration of voids and solid) and the properties of the solid constituent (e.g., stiffness, strength, etc.). In the ultralight regime below 10 mg/cm^3, very few materials currently exist: silica aerogels [density $\rho \geq 1$ mg/cm^3 (*1*, *2*)], carbon nanotube aerogels [$\rho \geq 4$ mg/cm^3 (*3*)], metallic foams [$\rho \geq 10$ mg/cm^3 (*4*, *5*)], and polymer foams [$\rho \geq 8$ mg/cm^3 (*6*, *7*)]. These materials have a wide range of applications, such as thermal insulation, shock or vibration damping, acoustic absorption, and current collectors in battery electrodes and catalyst supports (*8*). All of the ultralow-density materials mentioned above have random cellular architectures. This random cell structure results in some beneficial properties (e.g., high specific surface area and restriction of gas flow), but generally the inefficient distribution of the constituent results in specific properties (e.g., stiffness, strength, energy absorption, and conductivity) far below those of the bulk material (*8*). As an example, Young's modulus, E, of ultralight stochastic materials scales poorly with density, generally following $E \sim \rho^3$ (*9*), in contrast to the well-known $E \sim \rho^2$ relationship for random open-cell foams with higher relative densities (*8*). In large-scale structures, it has been shown that introducing order and hierarchy can substantially improve material utilization and resultant properties. For instance, the Eiffel Tower possesses a relative density similar to that of low-density aerogels (*10*) but is clearly structurally robust. The size difference between the smallest and largest structural features will determine the degree of hierarchy that can be achieved. In this paper, we present a method for creating ordered hollow-tube lattice materials with a minimum scale of ~100 nm. Coupled with control over μm- to cm-scale structural features, this enables us to bring the benefits of order and hierarchy down to the materials level. The result is an ultralightweight cellular material with efficient material utilization, a Young's modulus that follows $E \sim \rho^2$, and the ability to recover from >50% compression while demonstrating large energy absorption upon cyclic loading.

The base architecture of our metallic microlattices consists of a periodic array of hollow tubes that connect at nodes, forming an octahedral unit cell without any lattice members in the basal plane. Figure 1 illustrates how the microlattice architecture can be distilled into three levels of hierarchy at three distinct length scales: unit cell (~mm to cm), hollow tube lattice member (~μm to mm), and hollow tube wall (~nm to μm). Each architectural element can be controlled independently, providing exceptional control over the design and properties of the resulting microlattice. The architecture determines the relative density of the lattice, with the absolute density dictated by the film material.

The fabrication process begins with solid microlattice templates fabricated by using a self-propagating photopolymer waveguide technique. In this method, a thiol-ene liquid photomonomer is exposed to collimated ultraviolet (UV) light through a patterned mask, producing an interconnected three-dimensional photopolymer lattice (*11*). A wide array of different architectures with unit cell dimensions ranging from 0.1 to >10 mm can be made by altering the mask pattern and the angle of the incident light (*12*, *13*). Here, we focus on architectures with 1- to 4-mm lattice member length L, 100- to 500-μm lattice member diameter D, 100- to 500-nm wall thickness t, and 60° inclination angle θ, similar to the microlattices depicted in Fig. 1. Conformal nickel-phosphorous thin films were deposited on the polymer lattices by electroless plating, and the polymer was subsequently etched out (table S1). The autocatalytic electroless nickel-plating reaction enables deposition of thin films with controlled thickness on complex shapes and inside pores without noticeable mass transport limitations. The ultralight microlattice essentially translates the deposited nanoscale thin film in three dimensions to form a macroscopic material where the base structural elements are hollow tubes. By controlling the reaction time, a 100-nm-thick uniform conformal coating can be achieved, resulting in a cellular material with a density of 0.9 mg/cm^3 (Fig. 1). The density is calculated by using the weight of the solid structure but not including the

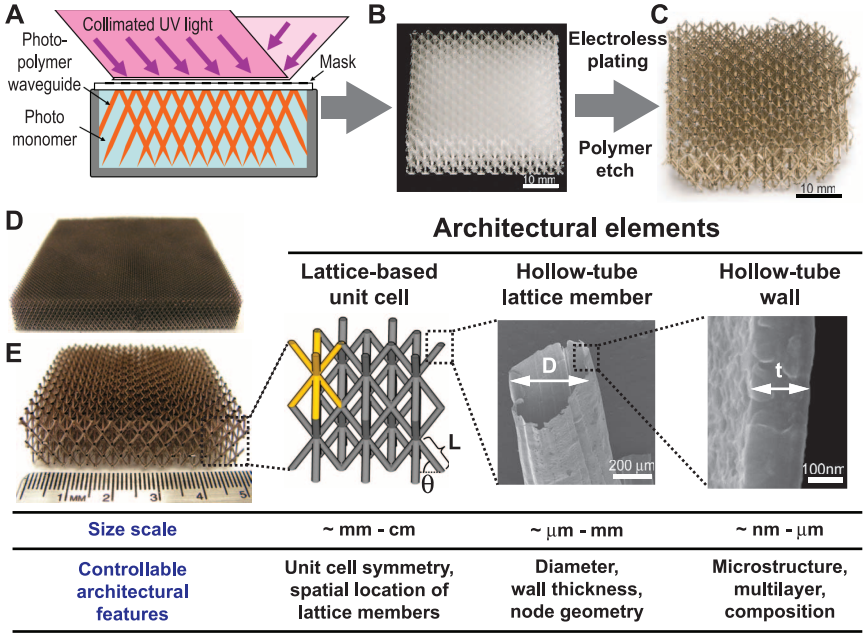

Fig. 1. Design, processing, and cellular architecture of ultralight microlattices. (**A**) Polymer microlattice templates are fabricated from a three-dimensional array of self-propagating photopolymer waveguides. (**B**) The open-cellular templates are electroless plated with a conformal Ni-P thin film followed by etch removal of the template. (**C**) Image of the lightest Ni-P microlattice fabricated with this approach: 0.9 mg/cm^3. (**D** and **E**) Images of two as-fabricated microlattices along with a breakdown of the relevant architectural elements.

[1]HRL Laboratories Limited Liability Company, Malibu, CA 90265, USA. [2]Department of Mechanical and Aerospace Engineering, University of California, Irvine, CA 92697, USA. [3]Division of Engineering and Applied Sciences, California Institute of Technology, Pasadena, CA 91125, USA.

*To whom correspondence should be addressed. E-mail: taschaedler@hrl.com

weight of air in the pores, adhering to the standard practice for cellular materials. The density of air at ambient conditions, 1.2 mg/cm^3, multiplied by its volume fraction would need to be added to express the density of the solid-air composite. This method to form microlattices allows significantly more control than typical methods for forming other ultralightweight materials, such as foams and aerogels, where nominally random processes govern porosity formation.

Characterization of the base constituent by transmission electron microscopy (TEM) revealed that as-deposited electroless nickel thin films have an average grain size of ~7 nm, which is consistent with literature reports (*14*, *15*). Energy-dispersive x-ray spectroscopy confirmed that the film composition is 7% phosphorous and 93% nickel by weight. Because the films were not annealed after deposition, they remained as a supersaturated solid solution of phosphorous in a crystalline face-centered cubic nickel lattice with no Ni_3P precipitates present (*14*). The 7-nm grain size renders electroless nickel thin films harder and more brittle than typical nano- and microcrystalline nickel. A hardness of 6 GPa and a modulus of 210 GPa were measured by nanoindentation and hollow tube compression experiments, respectively (*16*).

Compression experiments on the as-formed microlattices showed a nearly complete recovery

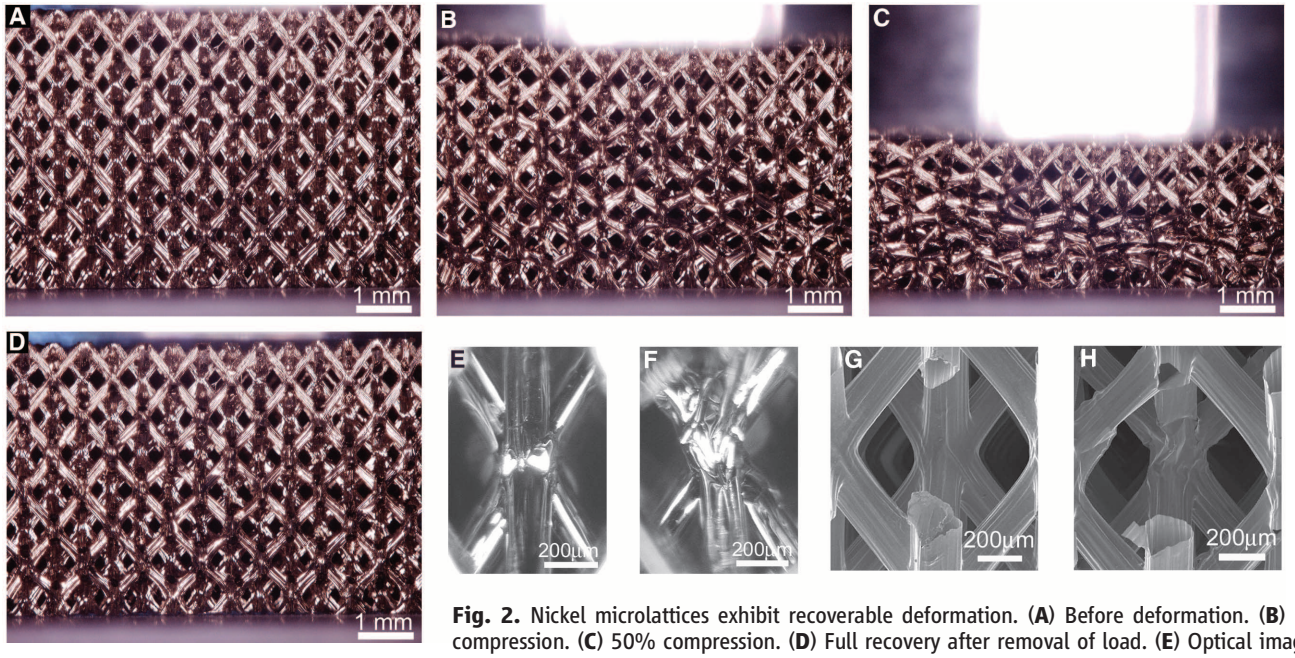

Fig. 2. Nickel microlattices exhibit recoverable deformation. (**A**) Before deformation. (**B**) 15% compression. (**C**) 50% compression. (**D**) Full recovery after removal of load. (**E**) Optical image of unit cell unloaded. (**F**) Example of node buckling under compression. (**G**) SEM image of node before testing. (**H**) SEM image of node after six compression cycles at 50% strain. (The compression test is shown in movie S1.)

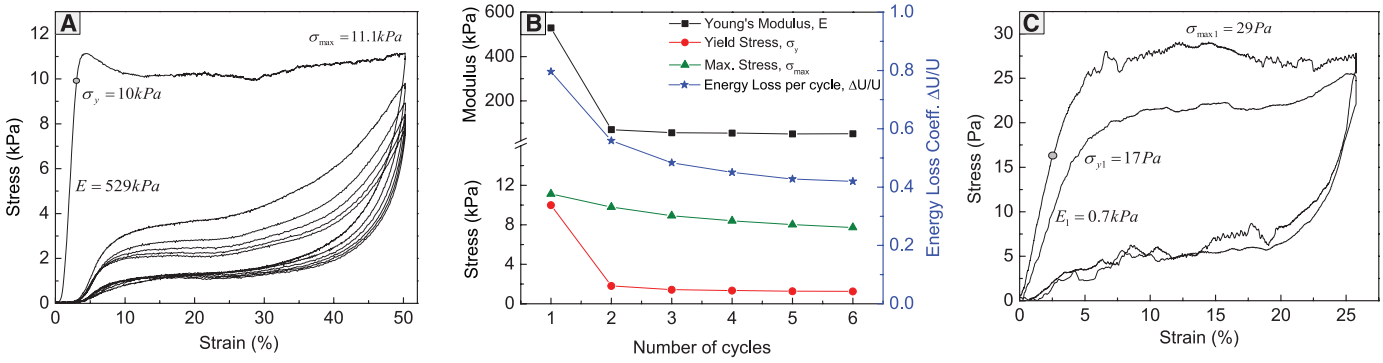

Fig. 3. Multicycle compression test results of nickel microlattices. (**A**) Stress-strain curves of a microlattice with 14 mg/cm^3 exhibiting recoverable deformation (compare with Fig. 2). (**B**) History of compressive modulus, yield stress, maximum stress, and energy loss coefficient during the first six compression cycles shown in (A). (**C**) Stress-strain curve of a microlattice with a density of 1.0 mg/cm^3. (**D**) Stress-strain curves of a microlattice with 43 mg/cm^3 showing deformation more typical for metallic cellular materials. (**E**) SEM micrograph of post-nanoindentation mark in 500-nm-thick electroless nickel film demonstrating brittle behavior.

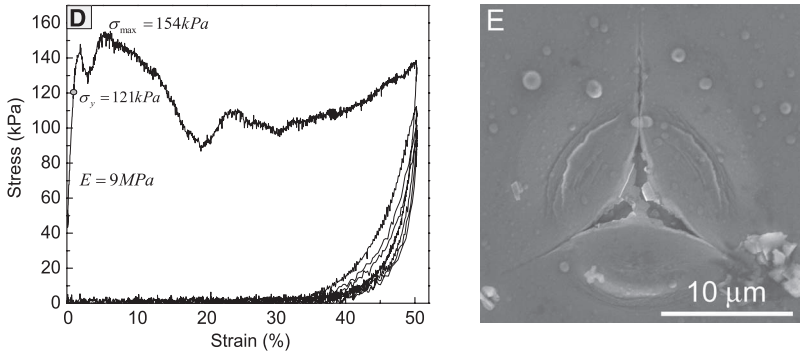

from strains exceeding 50% (movie S1). Figure 2, A to D, provides images of a 14 mg/cm^3 microlattice sample (L = 1050 μm, D = 150 μm, t = 500 nm) during compression testing, and Fig. 3A conveys the corresponding stress-strain curve measured at a prescribed displacement rate of 10 μm/s. In this experiment, the sample was not constrained by face sheets or attached to any compression platens. Because of a small taper in lattice strut diameter, the deformation typically initiates at a particular surface. Upon first compression, the lattice exhibits a compressive modulus of 529 kPa, with deviations from linear elastic behavior starting at ~10 kPa. The stress decreases slightly after the peak, which is associated with buckling and node fracture events, and a broad plateau is subsequently established in the stress-strain curve as buckling and localized node fracture events spread through the lattice. Figure 2C shows the microlattice at 50% compression. Upon unloading, the stress drops rapidly but does not approach zero until the platen is close to its original position. After removing the load, the microlattice recovers to 98% of its original height and resumes its original shape (Figs. 2D and 3A).

The stress-strain behavior corresponding to the first cycle is never repeated during subsequent testing. Rather, during a second compression, the peak stress is absent and the "pseudohardening" behavior changes, but the stress level achieved at 50% strain is only 10% lower than that after the first cycle. Consecutive compression cycles exhibit stress-strain curves nearly identical to those of the second compression. Stiffness and strength diminish with cycle number but remain almost constant after the third cycle (Fig. 3B). The microlattice also shows significant hysteresis during compression experiments. For the first cycle, we estimate the work done in compression to be 4.6 mJ/cm^3 and the energy dissipation to be 3.5 mJ/cm^3, yielding an energy loss coefficient ($\Delta u/u$) of 0.77. This large energy dissipation results from extensive node microcracking and thus is limited to the first cycle. After three cycles, a nearly constant energy loss coefficient of ~0.4 is calculated (Fig. 3B). From this estimate, we extract a loss coefficient (tan δ) of ~0.16 (*17*), an order of magnitude higher than for typical nickel foams (*18*). Figure 3C shows the stress-strain response of a 1.0 mg/cm^3 sample with larger unit cells (L = 4 mm, D = 500 μm, t = 120 nm), illustrating that different microlattice architectures in the ultralow-density regime result in similar behavior [although this sample underwent an additional freeze-drying process step that caused some damage (table S1)]. Increasing the density and wall thickness eventually led to a compression behavior more typical for metallic cellular materials. Figure 3D shows the stress-strain curve for a 43-mg/cm^3 sample (L = 1050 μm, D = 150 μm, t = 1400 nm), for which recovery upon unloading from 50% strain is essentially absent.

Optical examination of the ultralight microlattices during deformation suggests that deformation initiates by local buckling at the nodes (Fig. 2, E and F). A closer inspection of the microlattices by scanning electron microscopy (SEM) shows that cracks and wrinkles are introduced primarily at the nodes during compression (Fig. 2, G and H). This damage is responsible for the 1 to 2% residual strain observed after the first compression cycle, as well as for the drop in yield strength and modulus during subsequent compression cycles. Once stable "relief cracks" form at the nodes, the bulk microlattice material can undergo large effective compressive strains through extensive rotations about remnant node ligaments, but with negligible strain in the solid nickel-phosphorous material, thus requiring no further fracture or plastic deformation. This property results in the reversible compressive behavior shown in Figs. 2 and 3. The extremely small wall thickness–to–diameter ratio is essential for this deformation mechanism. Increasing this aspect ratio leads to excessive fracture and loss of recoverability (Fig. 3D).

The rise in stress at strains of ~40% (Fig. 3A) is a result of increased interaction between lattice members after localized compression at the nodes and should not be confused with densification, which in these samples does not occur until strains exceed 90% (fig. S2).

Similar stress-strain curves as presented in Fig. 3A are typical for viscoelastic polymer foams (*19*) and carbon nanotube forests (*20*) but not for metal-based materials, implying a nonconventional loss mechanism is present. Two energy-loss mechanisms could possibly explain the energy dissipation during compression cycles: (i) structural damping because of snapping events (e.g., kinking or local buckling of the trusses) and (ii) mechanical or Coulomb friction between contacting members (or a combination of both). This mechanical behavior is especially unexpected considering the relatively brittle nature of the constituent electroless nickel thin film, as evidenced by the formation of cracks near a residual indentation mark (Fig. 3E) and the rapid collapse upon single hollow truss member compressions (*16*). The brittle nature of the film arises from its nanograined microstructure (~7 nm) that hinders plastic deformation by dislocation motion (*21*). However, at the bulk scale microlattices exhibit completely different properties, because the cellular architecture effectively transforms this brittle thin film into a ductile, superelastic lattice by enabling sufficient freedom for deformation and tolerance to local strains through formation of stable relief cracks.

Plotting the relative compressive modulus, E/E_s, of various fabricated microlattices versus their relative density, ρ/ρ_s, shows that the modulus scales with $(\rho/\rho_s)^2$ (Fig. 4). This scaling law indicates bending-dominated mechanical behavior similar to open-cell stochastic foams (*8*). In contrast, other materials with densities < 10 mg/cm^3, such as aerogels and carbon nanotube (CNT) foams, exhibit a steeper scaling of $E/E_s \sim (\rho/\rho_s)^3$ (Fig. 4) (*22*, *23*), because of inefficient load transfer between ligaments. (Incidentally, this also affects the structural stability of a self-supporting cellular material, imposing a lower bound on density.) We notice that, although the relative modulus of topologically designed periodic lattice materials [such as octet-truss lattices (*24*)] typically scales linearly with relative density (*25*, *26*), we do not expect the same scaling for the microlattices described here because of the absence of struts in the basal plane (*26*) and the ultrathin-walled hollow nodes, both of which facilitate localized bending deformation (Fig. 2F). Nonetheless, the marked improvement in mechanical efficiency over any other existing ultralightweight material, achieved by controlling both dimensions and periodicity of the architecture, enabled a self-supporting cellular material with a relative density an order of magnitude lower than previously realized. Further, by transforming a brittle Ni-P thin film into a three-dimensional cellular material and designing a hierarchical cellular architecture at three

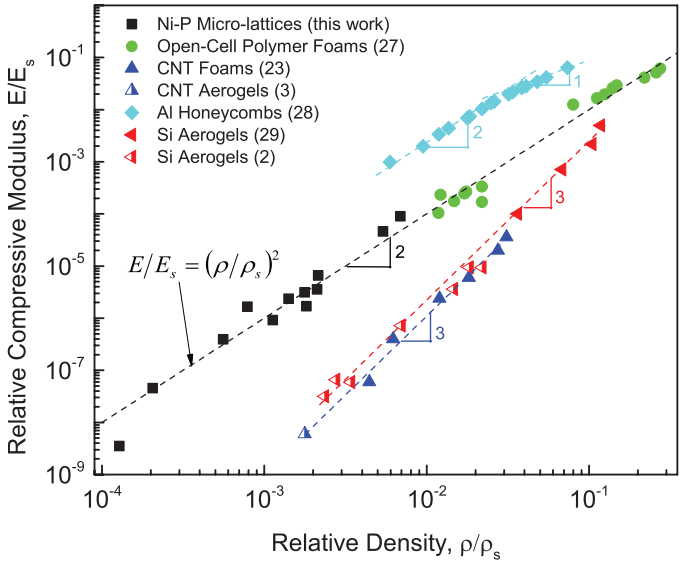

Fig. 4. Relative compressive modulus (defined as the measured Young's modulus, E, divided by the Young's modulus of the constituent solid, E_s) of selected cellular materials at low relative density.

distinct length scales, we demonstrated the emergence of entirely different mechanical properties. In addition to possible applications for an ultralight material with high energy absorption and recoverability, we anticipate that these results will help reshape our understanding of the interaction between material properties and structural architecture.

References and Notes

1. Guinness Book of World Records, Least Dense Solid (2003), www.guinnessworldrecords.com/records-1/least-dense-solid/.
2. T. M. Tillotson, L. W. Hrubesh, *J. Non-Cryst. Solids* **145**, 44 (1992).
3. J. Zou *et al*., *ACS Nano* **4**, 7293 (2010).
4. A. Verdooren, H. M. Chan, J. L. Grenestedt, M. P. Harmer, H. S. Caram, *J. Am. Ceram. Soc.* **89**, 3101 (2006).
5. B. C. Tappan *et al*., *J. Am. Chem. Soc.* **128**, 6589 (2006).
6. M. Chanda, S. K. Roy, *Plastics Technology Handbook* (CRC Press, Boca Raton, FL, 2007).
7. B. A. S. F. Corporation, Materials Safety Data Sheet for Basotect V3012 (2007), www.basf.co.kr/02_products/01_thermoplastics/spe/document/MSDS-Basotect%20V3012.pdf.
8. L. J. Gibson, M. F. Ashby, *Cellular Solids: Structure and Properties* (Cambridge Univ. Press, Cambridge, 1997).
9. H.-S. Ma, J.-H. Prévost, R. Jullien, G. W. Scherer, *J. Non-Cryst. Solids* **285**, 216 (2001).
10. R. S. Lakes, *Nature* **361**, 511 (1993).
11. A. J. Jacobsen, W. Barvosa-Carter, S. Nutt, *Acta Mater.* **55**, 6724 (2007).
12. A. J. Jacobsen, W. Barvosa-Carter, S. Nutt, *Adv. Mater.* **19**, 3892 (2007).
13. A. J. Jacobsen, W. Barvosa-Carter, S. Nutt, *Acta Mater.* **56**, 2540 (2008).
14. S. H. Park, D. N. Lee, *J. Mater. Sci.* **23**, 1643 (1988).
15. S. Y. Chang, Y. S. Lee, H. L. Hsiao, T. K. Chang, *Metall. Mater. Trans. A* **37A**, 2939 (2006).
16. J. Lian *et al*., *Nano Lett.* **11**, 4118 (2011).
17. G. F. Lee, B. Hartmann, *J. Sound Vibrat.* **211**, 265 (1998).
18. M. F. Ashby *et al*., *Metal Foams: A Design Guide* (Butterworth-Heinemann, Burlington, MA, 2000), p. 43.
19. N. J. Mills, *Cell. Polym.* **5**, 293 (2006).
20. A. Cao, P. L. Dickrell, W. G. Sawyer, M. N. Ghasemi-Nejhad, P. M. Ajayan, *Science* **310**, 1307 (2005).
21. J. R. Trelewicz, C. A. Schuh, *Acta Mater.* **55**, 5948 (2007).
22. J. Gross, T. Schlief, J. Fricke, *Mater. Sci. Eng. A* **168**, 235 (1993).
23. M. A. Worsley, S. O. Kucheyev, J. H. Satcher Jr., A. V. Hamza, T. F. Baumann, *Appl. Phys. Lett.* **94**, 073115 (2009).
24. V. S. Deshpande, N. A. Fleck, M. F. Ashby, *J. Mech. Phys. Solids* **49**, 1747 (2001).
25. V. S. Deshpande, M. F. Ashby, N. A. Fleck, *Acta Mater.* **49**, 1035 (2001).
26. V. S. Deshpande, N. A. Fleck, *Int. J. Solids Struct.* **38**, 6275 (2001).
27. L. J. Gibson, M. F. Ashby, *Proc. R. Soc. London Ser. A* **382**, 43 (1982).
28. Hexcel Corporation, *HexWeb Honeycomb Attributes and Properties* (1999); datasheet available at www.hexcel.com/Resources/DataSheets/Brochure-Data-Sheets/Honeycomb_Attributes_and_Properties.pdf.
29. M. Moner-Girona, A. Roig, E. Molins, E. Martinez, J. Esteve, *Appl. Phys. Lett.* **75**, 653 (1999).

Acknowledgments: The authors gratefully acknowledge the financial support by Defense Advanced Research Projects Agency under the Materials with Controlled Microstructural Architecture program managed by J. Goldwasser (contract no. W91CRB-10-0305) and thank J. W. Hutchinson and C. S. Roper for useful discussions. A patent application regarding the structure and formation process of the ultralight microlattices has been submitted to the U.S. Patent and Trademark Office. The polymer waveguide process has been patented (U.S. Patent 7,382,959, U.S. Patent 7,653,279, and U.S. Patent 8,017,193), but the template can be fabricated in other ways.

Supporting Online Material

www.sciencemag.org/cgi/content/full/334/6058/962/DC1
Materials and Methods
Fig. S1
Table S1
References
Movie S1

25 July 2011; accepted 12 October 2011
10.1126/science.1211649

Silica-Like Malleable Materials from Permanent Organic Networks

Damien Montarnal, Mathieu Capelot, François Tournilhac, Ludwik Leibler*

Permanently cross-linked materials have outstanding mechanical properties and solvent resistance, but they cannot be processed and reshaped once synthesized. Non–cross-linked polymers and those with reversible cross-links are processable, but they are soluble. We designed epoxy networks that can rearrange their topology by exchange reactions without depolymerization and showed that they are insoluble and processable. Unlike organic compounds and polymers whose viscosity varies abruptly near the glass transition, these networks show Arrhenius-like gradual viscosity variations like those of vitreous silica. Like silica, the materials can be wrought and welded to make complex objects by local heating without the use of molds. The concept of a glass made by reversible topology freezing in epoxy networks can be readily scaled up for applications and generalized to other chemistries.

Thermoset polymers such as Bakelite must be polymerized in a mold having the shape of the desired object because once the reaction is completed, the polymer cannot be reshaped or reprocessed by heat or with solvent. In contrast, thermoplastics, when heated, can flow, which permits extrusion, injection, and molding of objects. Depending on the chemical nature of the plastic, during cooling, solidification occurs by crystallization or by glass transition. During vitrification, as the temperature is lowered below the glass transition, the viscosity abruptly increases in a narrow temperature range, and the material becomes so viscous that it behaves essentially like a solid with an elastic modulus of about 10^9 to 10^{10} Pa (*1*). Nevertheless, compared to processable plastics, cross-linked polymers have superior dimensional stability; have high-temperature mechanical, thermal, and environmental resistance; and are irreplaceable in many demanding applications, such as in the aircraft industry. High-performance coatings, adhesives, rubbers, light-emitting diode lenses, and solar cell encapsulants are made of permanently cross-linked polymer networks as well.

Making covalent links reversible could provide a way to combine processability, reparability, and high performance (*2*–*6*). Networks with bonds able to break and reform (*7*–*9*) or to exchange pairs of atoms (*10*) can relax stresses and flow. The challenge is to allow rapid reversible reactions at high temperatures or by a convenient stimulus and to fix the network at service conditions. In this context, cleavage or exchange reactions by addition-fragmentation in the presence of radicals offer interesting possibilities (*5*, *11*–*14*). Scott *et al*. demonstrated photoinduced plasticity in cross-linked polymers (*11*). Similarly, reparability and self-healing can be induced either thermally (*13*) or photochemically (*15*, *16*) in radical systems. However, these systems undergo unavoidable termination reactions that limit reversibility of the networks.

In parallel, a completely different concept based on chemical equilibrium between bond breaking and reforming without irreversible side reactions has been developed (*17*–*20*). In these systems, heating has two effects: It displaces the equilibrium toward depolymerization and it accelerates the bond breaking and reforming rate (*8*, *9*). The advantage of such reversible links is that both above-mentioned effects act together to bring fluidity and thus processability (*5*, *17*–*19*). They are, however, detrimental to the network integrity and performance. Chen *et al*. have shown that to avoid flow and creep at service temperatures, one can rely, as in thermoplastics, on glass transition to quench the system (*17*). Unfortunately, the systems based on chemical equilibrium between bond breaking and reforming are sensitive to solvents because in the presence of a solvent, the chemical equilibrium is displaced toward network depolymerization and dissolution (*19*).

We sought to show that reversible networks can flow while maintaining their integrity and insolubility at high temperature. The idea is to

Matière Molle et Chimie, UMR 7167 CNRS-ESPCI, Ecole Supérieure de Physique et Chimie Industrielles, 10 rue Vauquelin, 75005 Paris, France.

*To whom correspondence should be addressed. E-mail: ludwik.leibler@espci.fr